A&A 624, A74 (2019)
https://doi.org/10.1051/0004-6361/201935075

Astronomy & Astrophysics

Plasma environment effects on K lines of astrophysical interest

I. Atomic structure, radiative rates, and Auger widths of oxygen ions

J. Deprince[1], M. A. Bautista[2], S. Fritzsche[3,4], J. A. García[5,6], T. R. Kallman[7], C. Mendoza[2], P. Palmeri[1], and P. Quinet[1,8]

[1] Physique Atomique et Astrophysique, Université de Mons – UMONS, 7000 Mons, Belgium
e-mail: patrick.palmeri@umons.ac.be
[2] Department of Physics, Western Michigan University, Kalamazoo, MI 49008, USA
[3] Helmholtz Institut Jena, 07743 Jena, Germany
[4] Theoretisch Physikalisches Institut, Friedrich Schiller Universität Jena, 07743 Jena, Germany
[5] Cahill Center for Astronomy and Astrophysics, California Institute of Technology, Pasadena, CA 91125, USA
[6] Dr. Karl Remeis-Observatory and Erlangen Centre for Astroparticle Physics, Sternwartstr. 7, 96049 Bamberg, Germany
[7] NASA Goddard Space Flight Center, Code 662, Greenbelt, MD 20771, USA
[8] IPNAS, Université de Liège, Sart Tilman, 4000 Liège, Belgium

Received 17 January 2019 / Accepted 4 March 2019

ABSTRACT

Aims. In the context of black-hole accretion disks, the main goal of the present study is to estimate the plasma environment effects on the atomic structure and radiative parameters associated with the K-vacancy states in ions of the oxygen isonuclear sequence.
Methods. We used a time-averaged Debye–Hückel potential for both the electron–nucleus and the electron–electron interactions implemented in the fully relativistic multiconfiguration Dirac–Fock (MCDF) method.
Results. Modified ionization potentials, K thresholds, Auger widths, and radiative transition wavelengths and rates are reported for O I–O VII in plasma environments with electron temperature and density ranges 10^5–10^7 K and 10^{18}–10^{22} cm^{-3}.

Key words. black hole physics – plasmas – atomic data – X-rays: general

1. Introduction

High-density plasma effects (free–free heating at electron densities $n_e > 10^{19}$ cm^{-3}) may explain the apparent supersolar Fe abundances inferred from the X-ray spectra of accreting black holes (García et al. 2018). However, the currently available atomic data to model astronomical spectra do not take into account high-density effects, and are therefore limited to densities below 10^{18} cm^{-3} (García et al. 2016). In regard to this, Schnittman et al. (2013) recently carried out magnetohydrodynamic (MHD) simulations of a 10 $M_\odot$ black hole accreting at a 10% rate, and predicted plasma conditions in the accretion disk characterized by electron temperatures and densities spanning the ranges 10^5–10^7 K and 10^{18}–10^{22} cm^{-3}. Fields et al. (2007) have determined supersolar abundances for carbon, nitrogen, oxygen, and iron from a high-resolution *Chandra* spectrum of the warm absorbing gas outflowing from the active galactic nucleus (AGN) Mrk 279 compact region, where especially the oxygen abundance is estimated at approximately eight times solar. This latter environment type is also expected to have densities greater than 10^{19} cm^{-3}.

García et al. (2005) reported a complete set of atomic data relevant to the modeling of oxygen K lines formed in astrophysical photoionized plasmas. As underlined by Smith & Brickhouse (2014) in the interpretation of X-ray spectra taken by current space observatories, none of these atomic parameters take into account high-density plasma embedding, where the atomic structure and processes (e.g., emissivities, opacities, and ionization balance) could be significantly distorted by the extreme temperature and density.

In the present study we provide a complete set of structure and radiative data for the modeling of oxygen K lines that include plasma environment effects. In Sect. 2, we describe the atomic physics computational approach, and in Sect. 3 we validate the time-averaged potential used to model the plasma environment by means of three test cases. In Sect. 4 we discuss in detail our results, and finally our conclusions are drawn in Sect. 5.

2. Theoretical approach

In the multiconfiguration Dirac–Fock (MCDF) method (Grant et al. 1980; McKenzie et al. 1980; Grant 1988) the atomic state function (ASF) Ψ is represented by a linear combination of configuration state functions (CSF) Φ of the same parity (P), total angular momentum (J), and angular-momentum projection (M)

$$\Psi(\gamma, P, J, M) = \sum_i c_i \, \Phi(\alpha_i, P, J, M), \tag{1}$$

where the CSFs are antisymmetrized products of orthonormal monoelectronic spin-orbitals of the form

$$\varphi_{n\kappa m}(r, \theta, \phi) = \frac{1}{r} \begin{pmatrix} P_{n\kappa}(r)\, \chi_{\kappa m}(\theta, \phi) \\ i\, Q_{n\kappa}(r)\, \chi_{-\kappa m}(\theta, \phi) \end{pmatrix}. \tag{2}$$

In Eq. (2) $P_{n\kappa}(r)$ and $Q_{n\kappa}(r)$ are the large and small radial orbitals, respectively, and the angular functions $\chi_{\kappa m}(\theta, \phi)$ are spinor spherical harmonics. These spin-orbitals are optimized self-consistently based on the Dirac–Coulomb Hamiltonian

$$H_{\rm DC} = \sum_i c\boldsymbol{\alpha_i} \cdot \boldsymbol{p_i} + \beta_i c^2 - \frac{Z}{r_i} + \sum_{i>j} \frac{1}{r_{ij}}. \quad (3)$$

For an atom embedded in a weakly coupled plasma, the Hamiltonian of Eq. (3) is replaced with the Debye–Hückel (DH) screened Dirac–Coulomb Hamiltonian (Saha & Fritzsche 2006)

$$H_{\rm DC}^{\rm DH} = \sum_i c\boldsymbol{\alpha_i} \cdot \boldsymbol{p_i} + \beta_i c^2 - \frac{Z}{r_i} e^{-\mu r_i} + \sum_{i>j} \frac{1}{r_{ij}} e^{-\mu r_{ij}}, \quad (4)$$

where $r_{ij} = |\boldsymbol{r}_i - \boldsymbol{r}_j|$ and the plasma screening parameter μ is the inverse of the Debye shielding length $\lambda_{\rm D}$, which can be expressed in atomic units (au) as a function of the plasma electron density $n_{\rm e}$ and temperature $T_{\rm e}$ as

$$\mu = \frac{1}{\lambda_D} = \sqrt{\frac{4\pi n_{\rm e}}{kT_{\rm e}}}. \quad (5)$$

Typical plasma conditions in black-hole accretion disks are $T_{\rm e} \sim 10^5$–10^7 K and $n_{\rm e} \sim 10^{18}$–10^{22} cm^{-3} (Schnittman et al. 2013). For weakly coupled plasmas they correspond to screening parameters $0.0 \le \mu \le 0.24$ au and, for a completely ionized hydrogen plasma (with plasma ionization $Z^* = 1$), to plasma coupling parameters

$$\Gamma = \frac{e^2}{4\pi\epsilon_0 d k T_{\rm e}}, \quad (6)$$

with

$$d = \left(\frac{3}{4\pi n_{\rm e}}\right)^{1/3}, \quad (7)$$

in the range $0.0003 \le \Gamma \le 0.6$.

The last term of Eq. (4) has the angular dependence (Saha & Fritzsche 2006)

$$\frac{1}{r_{ij}} {\rm e}^{-\mu r_{ij}} = -\mu \sum_{l=0}^{\infty} (2l+1)\; j_{\rm l}(i\mu r_<)\; h_{\rm l}^1(i\mu r_>)\; P_{\rm l}(\cos\omega_{ij}), \quad (8)$$

where $r_> = \max(r_i, r_j)$, $r_< = \min(r_i, r_j)$, $j_{\rm l}$ is a Bessel function, $h_{\rm l}^1$ denotes a Hankel function of the first kind, and $P_{\rm l}$ is a Legendre polynomial that depends on the angle ω_{ij} between the two position vectors $\boldsymbol{r}_i$ and $\boldsymbol{r}_j$. This screening reduces the electron–electron repulsion and, hence, increases the binding of the electron by the nucleus.

We use the active space (AS) method to obtain the MCDF expansions of Eq. (1) for O I–O VII, whereby electrons from reference configurations are excited to a given active set of orbitals. For these oxygen ions, the AS was built up by considering all the single and double excitations of the reference configurations listed for each species in Table 1 to configurations including $n = 2$ and $n = 3$ orbitals.

In the isolated atom approximation, the relativistic orbitals $P_{n\kappa}(r)$ and $Q_{n\kappa}(r)$, along with the expansion coefficients c_i in Eqs. (1)–(2), were optimized using the GRASP2K package (Parpia et al. 1996) with the extended average level (EAL) option, where the $(2J+1)$-weighted trace of the Dirac–Coulomb Hamiltonian (see Eq. (3)) is minimized to determine energy levels, wavelengths, and radiative and Auger rates. To take into account core-relaxation effects on the K-vacancy states (García et al. 2005), we introduce non-orthogonal orbitals optimized separately in two distinct level groups: a first group of exclusively valence levels where the K shell is full; and a second group of levels with at least a single K-vacancy. For the ionization potential (IP) and K threshold, the orbitals were respectively optimized on the ground level and on the lowest K-vacancy level of each ion using the optimal level (OL) option of GRASP2K.

Plasma effects are included perturbatively in a second step where we use the RATIP code of Fritzsche (2012) to improve the expansion coefficients, that is, the ASF, energy levels, and radiative rates, by solving the secular equation with the Debye–Hückel screened Dirac–Coulomb Hamiltonian (Eq. (4)), the two-body Breit interaction, and the quantum electrodynamic corrections (self-energy and vacuum polarization). Plasma screening parameters in the range $0.00 \le \mu \le 0.25$ au were adopted, the upper-limit choice, justified in Sect. 3.3, corresponding to the extreme plasma conditions found in accretion disks.

Table 1. Reference configurations used to build up the MCDF active space for O I–O VII.

Ion	Reference configurations
O I	$2p^4$, $[2s]2p^5$, $[2s]^2 2p^6$, $[1s]2p^5$, $[1s][2s]2p^6$
O II	$2p^3$, $[2s]2p^4$, $[2s]^2 2p^5$, $[1s]2p^4$, $[1s][2s]2p^5$, $[1s][2s]^2 2p^6$
O III	$2p^2$, $[2s]2p^3$, $[2s]^2 2p^4$, $[1s]2p^3$, $[1s][2s]2p^4$, $[1s][2s]^2 2p^5$
O IV	$2p$, $[2s]2p^2$, $[2s]^2 2p^3$, $[1s]2p^2$, $[1s][2s]2p^3$, $[1s][2s]^2 2p^4$
O V	$2s^2$, $2s2p$, $2p^2$, $[1s]2s^2 2p$, $[1s]2s2p^2$, $[1s]2p^3$
O VI	$2s$, $2p$, $[1s]2s2p$, $[1s]2p^2$
O VII	$1s^2$, $1s2s$, $1s2p$

3. Validation of the Debye–Hückel model potential

Stark shifts of the dipole-allowed spectral lines emitted by an ion in a dense plasma have been measured. In a semi-classical picture, neighboring electrons and ions give rise to effective microscopic electric fields that result in level energy shifts due to induced dipole moments in the emitting ion. Alternatively, Stark shifts can also be predicted quantum-mechanically with a Debye–Hückel potential (Rozsnyai 1975). To test the validity of our Debye–Hückel model potential, we performed a series of calculations with the GRASP2K/RATIP code to compare with available laboratory Stark shifts. Such comparisons are common pratice (see, e.g., Rozsnyai 1975; Neiger & Griem 1976, and more recently Belkhiri et al. 2015). The three test cases investigated are detailed in the following Sects. 3.1–3.3.

3.1. Stark shifts in valence transitions of O II

Djenize et al. (1998) measured Stark shifts for the valence-shell transitions $2p^2 3s\ ^4P_{3/2}$–$2p^2 3p\ ^4D^o_{5/2}$ (λ4641.81) and $2p^2 3s\ ^4P_{1/2}$–$2p^2 3p\ ^4D^o_{3/2}$ (λ4638.85) in O II, respectively as 0.03 ± 0.02 Å and 0.05 ± 0.02 Å, at a temperature $T_{\rm e} = 54\,000$ K and density $n_{\rm e} = 2.8 \times 10^{17}$ cm^{-3}. To reproduce these shifts theoretically, we considered intravalence and core–valence correlations up to $n = 5$ to represent the respective ASFs in the two transitions. The MCDF shifts obtained with $\mu = 0.0017$ au are both 0.05 Å in good agreement with experiments. Moreover, if the DH screening of the electron–electron Coulomb potential is switched off (i.e., $\mu = 0$ in the last term of Eq. (4)), these

Table 2. Plasma screening parameter μ (au) for different electron temperatures T_e and densities n_e.

T_e (K)	n_e (cm^{-3})				
	10^{18}	10^{19}	10^{20}	10^{21}	10^{22}
10^5	$\mu = 0.0024$	$\mu = 0.0077$	$\mu = 0.024$	$\mu = 0.077$	$\mu = 0.24$
10^6	$\mu = 0.00077$	$\mu = 0.0024$	$\mu = 0.0077$	$\mu = 0.024$	$\mu = 0.077$
10^7	$\mu = 0.00024$	$\mu = 0.00077$	$\mu = 0.0024$	$\mu = 0.0077$	$\mu = 0.024$

shifts become much larger: 0.26 Å and 0.25 Å, respectively. This results confirm that the DH electron–electron plasma screening cannot be neglected. It should be also emphasized that Djenize et al. (1998) compared their measurements with the semi-classical calculations of Griem (1974) and Dimitrijević (1982) (see multiplet No. 1 in their Fig. 4). The three sets of Stark shifts (Djenize et al. 1998; Griem 1974; Dimitrijević 1982) disagree to each other, with the theoretical values having opposite signs and being about ∼0.15 Å (Griem 1974) and ∼−0.05 Å (Dimitrijević 1982). In that respect, our time-independent quantum model confirms the measurements of Djenize et al. (1998).

3.2. Stark shifts in valence transitions of Na I

The Stark shifts of the valence-shell Na I D doublet at 5889.95/5895.90 Å were measured in a plasma with T_e = 38 000 K and $n_e = 3.5\times10^{17}$ cm^{-3} (Sreckovic et al. 1996), resulting in 0.38 ± 0.09 Å and 0.41 ± 0.09 Å, respectively. Our MCDF calculations with μ = 0.0023 au including both intravalence and core–valence correlations ($n \leq 4$) give 0.43 Å and 0.51 Å, respectively, in satisfactory agreement with experiments. Again, if the electron–electron screening is neglected, the MCDF shifts are very different, at 4.42 Å and 4.50 Å.

3.3. Ti Kα line pressure shift

Our last test case concerns the Kα line $1s^2\ ^1S_0 - 1s2p\ ^1P^o_1$ of He-like Ti XXI at 4749.73 eV. Khattak et al. (2012) measured a line shift of 3.4 ± 1.0 eV, and inferred an electron temperature greater than ∼3 keV and an electron density exceeding 10^{24} cm^{-3} from a hydrodynamic simulation of their laser-produced plasma. This experimental shift was then reproduced theoretically using an ion-sphere model by Belkhiri et al. (2015) leading to an estimate of 3.4 eV at T_e = 3 keV and $n_e = 4.2\times10^{24}$ cm^{-3}. In the same plasma conditions adopted by Belkhiri et al. (2015), namely μ = 0.27 au, our MCDF-DH model yields a line shift of 3.3 eV in good agreement with both the measurements and the ion-sphere calculation. We are therefore confident to consider plasma parameters up to μ = 0.27 au.

4. Results and discussion

In the following Sects. 4.1–4.3 we examine the DH plasma screening effects on the oxygen K-line characteristics by considering screening parameters in the range $0 \leq \mu \leq 0.25$ au, which, as shown in Table 2, can be associated to electron temperatures and densities in the ranges $10^5 \leq T_e \leq 10^7$ K and $10^{18} \leq n_e \leq 10^{22}$ cm^{-3}.

4.1. Ionization potentials and K thresholds

The IPs (E_0) and K thresholds (E_K) for O ions determined with MCDF for three values of the plasma screening parameter – μ = 0, 0.1 and 0.25 au – are listed in Tables 3–4. For isolated species (μ = 0), the National Institute of Standards and Technology (NIST) IPs (Kramida et al. 2016) are reproduced to within 1% except for O I, for which only a 4% accuracy was attained due to the well-known slow convergence of the CI expansion (Eq. (1)) for neutrals. As expected, a substantial reduction of the absolute values of E_0 and E_K increasing with μ is obtained. For the case of μ = 0.1, we show in Table 3 that, if the electron–electron DH screening is neglected (μ = 0 in the last term of Eq. (4)), the continuum lowering, particularly for the low ionized species, is much larger yielding an unphysical negative IP for O I. We therefore stress again that the DH electron–electron screening is essential.

Table 3. Plasma screening effects on the IP $E_0(\mu)$ in oxygen ions determined with the MCDF method.

Ion	NIST[(a)]	MCDF			
	E_0	$E_0(0)$	$E_0(0.1)$	$E_0(0.1)^{(b)}$	$E_0(0.25)$
O I	13.61804(7)	13.07	10.33	−6.85	6.42
O II	35.12111(6)	35.00	29.68	14.65	22.30
O III	54.93554(12)	54.80	46.90	34.26	36.12
O IV	77.41350(25)	77.31	66.82	56.60	52.52
O V	113.8989(5)	112.81	99.75	92.04	82.14
O VI	138.1189(21)	138.04	122.41	117.21	101.37
O VII	739.32679(6)	739.86	720.99	718.32	693.36

Notes. IP E_0 is given in electronvolt and the screening parameter μ in au. [(a)]Kramida et al. (2016). [(b)]e–e screening switched off.

Table 4. Plasma screening effects on the K threshold $E_K(\mu)$ in oxygen ions computed with MCDF.

Ion	$E_K(0)$	$E_K(0.1)$	$E_K(0.25)$
O I	543.58	540.62	535.47
O II	570.89	565.31	556.49
O III	593.27	585.08	572.74
O IV	626.49	615.64	599.52
O V	664.10	650.57	630.58
O VI	699.64	683.44	659.64
O VII	739.86	720.99	693.36

Notes. K threshold E_K is given in electronvolt and the screening parameter μ in au.

In Fig. 1 we plot the trends of the IP lowering $\Delta E_0(\mu) = E_0(\mu) - E_0(\mu = 0)$ with $Z_{\rm eff} = Z - N + 1$, which are found to be practically linear except for $Z_{\rm eff}$ = 7 (O VII) due to the absence of the DH electron–electron screening. We also include for each species the DH limit $\Delta E_0^{\rm DH} \equiv -Z_{\rm eff}\,\mu$ as $\Gamma \to 0$ determined by Stewart & Pyatt (1966) and Crowley (2014). For O VII, $\Delta E_0^{\rm DH} = -47.6$ eV close to the MCDF IP lowering for μ = 0.25.

K-threshold lowering ($\Delta E_K(\mu) = E_K(\mu) - E_K(\mu = 0)$) trends with $Z_{\rm eff}$ are very similar to those of ΔE_0 as shown in Fig. 2, a predominantly linear decrease up to $\Delta E_K \approx \Delta E_0 \approx$

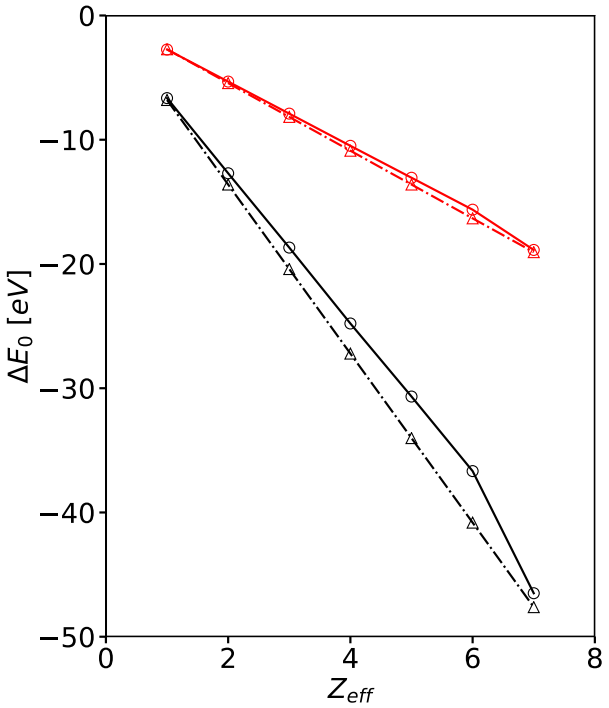

Fig. 1. IP lowering $\Delta E_0 = E_0(\mu) - E_0(\mu = 0)$ as function of the effective ionic charge $Z_{\rm eff} = Z - N + 1$ for two different values of μ. Circles: MCDF calculations. Triangles: DH limit ($\Delta E_0 = -Z_{\rm eff}\,\mu$). Red: $\mu = 0.1$ au. Black: $\mu = 0.25$ au. The broken trends observed for $Z_{\rm eff} = 7$ (O VII) in MCDF calculations are due to the absence of electron–electron plasma screening in the ground state of O VIII that contributes to the ionization potentials of O VII.

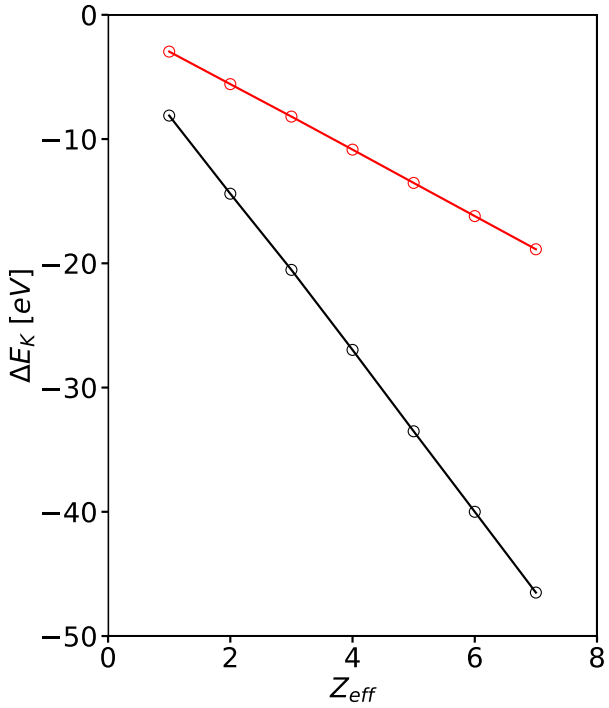

Fig. 2. MCDF K-threshold lowering $\Delta E_K = E_K(\mu) - E_K(\mu = 0)$ as function of the effective charge $Z_{\rm eff} = Z - N + 1$ for two different values of μ. Red: $\mu = 0.1$ au. Black: $\mu = 0.25$ au.

−50 eV. This finding is significant inasmuch as the DH screened photoionization cross sections will only involve approximately constant downward energy shifts of the thresholds leading to resonance series truncations rather than variant line wavelengths and resonance energy positions, points that are further discussed in Sects. 4.2–4.3.

4.2. Radiative data

Oxygen K-line wavelengths and transition probabilities (A-values) computed with MCDF with $\mu = 0$, 0.1 and 0.25 au are reported in Table A.1. For isolated systems ($\mu = 0$) our radiative data are in good general accord with the pseudo-relativistic Hartree–Fock (HFR) and multiconfiguration Breit–Pauli (MCBP) results of García et al. (2005); more precisely, present K-line wavelengths are shorter by 0.1% for the highly charged ions to little less than 1% for the lower ionization stages. In addition, they are in excellent agreement with the few spectroscopic reports available; for example, for the strong Kα line in O VII, our predicted wavelength agrees within 0.2% with the measurement by Engström & Litzén (1995), and within 0.7% and 0.2% with those reported by Schmidt et al. (2004) for O V and O VI, respectively. Regarding radiative rates, our MCDF results agree with García et al. (2005) on average to within 10% except for a few weak transitions.

Plasma effects on the radiative parameters are found to be small for $\mu = 0.1$ au but more conspicuous for $\mu = 0.25$ au (see Fig. 3). In fact for $\mu = 0.25$ au. K-line wavelengths appear to be shifted by ∼50−100 mÅ with respect to the isolated atom ($\mu = 0$) with a trend increasing with the ion effective charge $Z_{\rm eff}$ as shown in Fig. 3 (upper panel). Although small, such wavelength shifts can be resolved by present and next-generation satellite-borne X-ray spectrometers. The transition probabilities are generally also slightly modified; for instance, they are reduced on average by 5% with $\mu = 0.25$ au (see lower panel of Fig. 3), which would make negligible differences in astrophysical modeling.

4.3. K-vacancy level energies and Auger widths

Multiconfiguration Dirac–Fock level energies and Auger widths for oxygen K-vacancy levels are presented for $\mu = 0$, 0.1 and 0.25 au in Table A.2. Our MCDF energies for $\mu = 0$ au are slightly lower (∼0.5% on average) with respect to those computed with the HFR and MCBP by García et al. (2005), and our Auger widths are on average shorter by ∼25% and ∼20%, respectively. Level-energy decrements are in general found to be small ($|\Delta E| \lesssim 3.0$ eV) as illustrated in Fig. 4 (top panel) for $\mu = 0.1$ au and $\mu = 0.25$ au with trends increasing with $Z_{\rm eff}$. Regarding the Auger widths as shown in Fig. 4 (bottom panel), they are reduced on average by up to ∼10% for $\mu = 0.25$ au, which might have an impact on spectral K-line modeling. Neutral oxygen ($Z_{\rm eff} = 1$) has a different situation where MCDF predicts a 20% decrease for $\mu = 0.25$ au. This may illustrate the difficulty our atomic structure model has in computing accurate rates (better than 20%) at the neutral end of an isonuclear sequence.

5. Summary and conclusions

We have studied plasma embedding effects on the atomic structure of oxygen ions, namely the K-shell radiative parameters and Auger widths, as a function of the screening parameter. Such plasma effects were modeled perturbatively in the MCDF framework with a time-independent DH potential. Our main findings and conclusions can be summarized as follows:

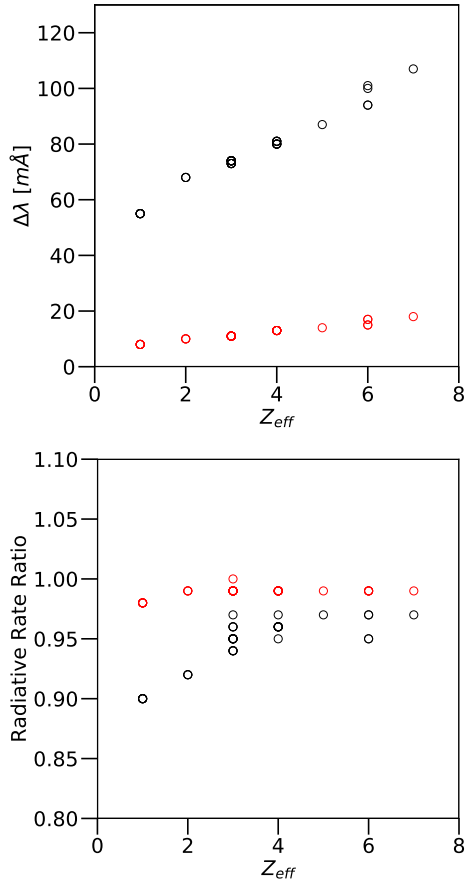

Fig. 3. *Top panel*: MCDF wavelength pressure shift $\Delta\lambda = \lambda(\mu) - \lambda(\mu = 0)$ for oxygen K lines as function of the effective charge $Z_{\rm eff} = Z - N + 1$ for two different values of μ. *Bottom panel*: MCDF radiative rate ratio $A(j,i,\mu)/A(j,i,\mu = 0)$ for oxygen K lines as function of the effective charge $Z_{\rm eff} = Z - N + 1$ for two different values of μ. Red: $\mu = 0.1$ au. Black: $\mu = 0.25$ au.

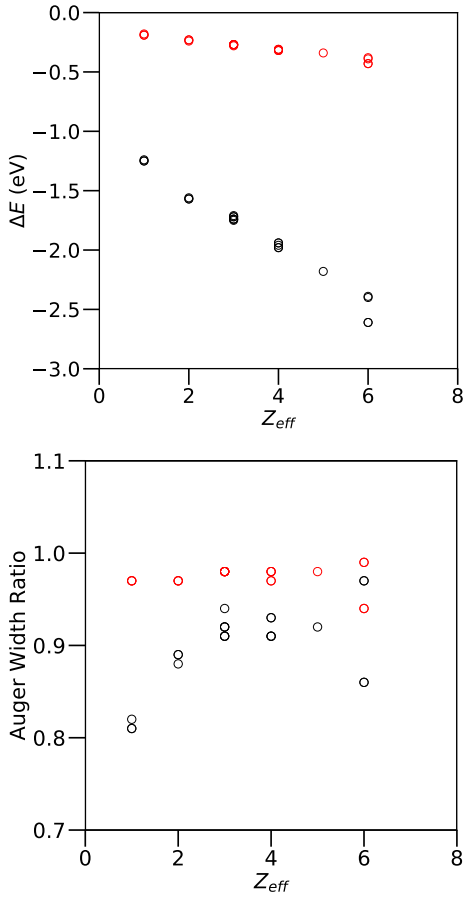

Fig. 4. *Top panel*: MCDF level-energy pressure shift $\Delta E = E(\mu) - E(\mu = 0)$ for oxygen K-vacancy levels as function of the effective charge $Z_{\rm eff} = Z - N + 1$ for two different values of μ. *Bottom panel*: MCDF Auger-width ratio $A_a(j,\mu)/A_a(j,\mu = 0)$ for oxygen K-vacancy levels as function of the effective charge $Z_{\rm eff} = Z - N + 1$ for two different values of μ. Red: $\mu = 0.1$ au. Black: $\mu = 0.25$ au.

1. The validity of our DH model has been benchmarked with Stark line-shift measurements (Sreckovic et al. 1996; Djenize et al. 1998; Khattak et al. 2012) for screening parameters as large as $\mu = 0.27$ au. The latter value has been associated with the extreme density conditions found in accretion disks around compact objects (see Table 2 and García et al. 2016). To obtain the desirable degree of agreement with experiments, the DH electron–electron screening must be taken into account.
2. We have studied plasma screening effects for $\mu \leq 0.25$ au finding considerable lowering (up to ∼50 eV) of both the IPs and K thresholds. Such shifts could arguably enhance the ionization fractions and K-vacancy state populations or, at least, lead to erroneous spectral line identifications.
3. Only a modest impact on the radiative and Auger data has been detected for $\mu \leq 0.1$ au, but it becomes more acute under the extreme plasma conditions of $\mu = 0.25$ au: K-line wavelengths are systematically redshifted by up to ∼0.1 Å with potential consequences on out- and inflow velocity determinations; and Auger rates might decrease by up to ∼20% in O I.
4. These new atomic data will be incorporated into the atomic the database of the XSTAR modeling code (Bautista & Kallman 2001) for future spectral analysis of accretion disks around compact objects.
5. We believe the perturbative approach adopted here for $\mu \leq 0.25$ is well supported by the relatively small effects on and smooth trends found in the atomic parameters, as well as by the good agreement with the experimentally determined Stark shifts for a few ionic species. More extreme conditions may require a non-perturbative inclusion of the DH potential; this work is underway and will be the subject of a subsequent report.

Acknowledgements. JD is a Research Fellow of the Belgian Fund for Research in Industry and Agriculture FRIA. PP & PQ are, respectively, Research Associate and Research Director of the Belgian Fund for Scientific Research F.R.S. –FNRS. Financial support from these organizations, as well as from the NASA Astrophysics Research and Analysis Program (grant 80NSSC17K0345) is gratefully acknowledged. We are indebted to Professor Nigel R. Badnell (Strathclyde University, UK) for lengthy and useful discussions on the validity of the Debye –Hückel potential and its implementations in atomic structure calculations. JAG acknowledges support from the Alexander von Humboldt Foundation.

References

Bautista, M. A., & Kallman, T. R. 2001, ApJS, 134, 139
Belkhiri, M., Fontes, C. J., & Poirier, M. 2015, Phys. Rev. A, 92, 032501
Crowley, B. J. B. 2014, High Energ. Dens. Phys., 13, 84
Djenize, S., Milosavljevic, V., & Sreckovic, A. 1998, J. Quant. Spectr. Rad. Trans., 59, 71
Dimitrijević, M. S. 1982, A&A, 112, 51

Engström, L., & Litzén, U. 1995, J. Phys. B: At. Mol. Opt. Phys., 28, 2565
Fields, D. J., Mathur, S., Krongold, Y., Williams, R., & Nicastro, F. 2007, ApJ, 666, 828
Fritzsche, S. 2012, Comput. Phys. Commun., 183, 1523
García, J., Mendoza, C., Bautista, M. A., Gorczyca, T. W., Kallman, T. R., & Palmeri, P. 2005, ApJS, 158, 68
García, J., Fabian, A. C., Kallman, T. R., et al. 2016, MNRAS, 462, 751
García, J., Kallman, T. R., Bautista, M., et al. 2018, ASP Conf. Ser., 515, 282
Grant, I. P. 1988, Meth. Comput. Chem., 2, 1
Grant, I. P., McKenzie, B. J., Norrington, P. H., Mayers, D. F., & Pyper, N. C. 1980, Comput. Phys. Commun., 21, 207
Griem, H. R. 1974, Spectral Line Broadening by Plasmas (Academic Press: New York)
Khattak, F. Y., Percie du Sert, O. A. M. B., Rosmej, F. B., & Riley, D. 2012, J. Phys. Conf. Ser., 397, 012020
Kramida, A., Ralchenko, Yu, Reader, J., & NIST ASD Team 2016, NIST Atomic Spectra Database (version 5.4) Available:http://physics.nist.gov/asd [Tue Oct 03 2017]. National Institute of Standards and Technology, Gaithersburg, MD
McKenzie, B. J., Grant, I. P., & Norrington, P. H. 1980, Comput. Phys. Commun., 21, 233
Neiger, M., & Griem, H. R. 1976, Phys. Rev. A, 14, 291
Parpia, F. A., Froese Fischer, C., & Grant, I. P. 1996, Comput. Phys. Commun., 94, 249
Rozsnyai, B. 1975, J. Quant. Spectr. Rad. Transf., 15, 695
Saha, B., & Fritzsche, S. 2006, Phys. Rev. E, 73, 036405
Schmidt, M., Beiersdorfer, P., Chen, H., Thorn, D. B., Träbert, E., & Behar, E. 2004, ApJ, 604, 562
Schnittman, J. D., Krolik, J. H., & Noble, S. C. 2013, ApJ, 769, 156
Smith, R. K., & Brickhouse, N. S. 2014, Adv. At. Mol. Opt. Phys., 63, 271
Sreckovic, A., Djenize, S., & Bukvic, S. 1996, Phys. Scr., 53, 54
Stewart, J. C., & Pyatt, Jr., K. D. 1966, ApJ, 144, 1203

Appendix A: Additional tables.

Table A.1. Plasma environment effects on the wavelengths and transition probabilities of Kα lines in oxygen ions computed with MCDF.

Ion	Transition	λ (Å)			$A(j,i)$ (s^{-1})		
		$\mu = 0.0$	$\mu = 0.1$	$\mu = 0.25$	$\mu = 0.0$	$\mu = 0.1$	$\mu = 0.25$
O I	$[1s]2p^5\ ^1P_1 - 2p^4\ ^1D_2$	23.3180	23.3252	23.3684	2.918E+12	2.885E+12	2.732E+12
	$[1s]2p^5\ ^3P_1 - 2p^4\ ^3P_2$	23.3752	23.3832	23.4301	6.648E+11	6.529E+11	5.993E+11
	$[1s]2p^5\ ^3P_0 - 2p^4\ ^3P_1$	23.3753	23.3833	23.4302	1.597E+12	1.568E+12	1.440E+12
	$[1s]2p^5\ ^3P_1 - 2p^4\ ^3P_1$	23.3759	23.3839	23.4308	3.992E+11	3.921E+11	3.601E+11
	$[1s]2p^5\ ^3P_1 - 2p^4\ ^3P_0$	23.3763	23.3843	23.4311	5.326E+11	5.231E+11	4.806E+11
	$[1s]2p^5\ ^3P_2 - 2p^4\ ^3P_2$	23.3763	23.3843	23.4312	1.197E+12	1.176E+12	1.080E+12
	$[1s]2p^5\ ^3P_2 - 2p^4\ ^3P_1$	23.3770	23.3851	23.4319	3.994E+11	3.924E+11	3.605E+11
	$[1s]2p^5\ ^1P_1 - 2p^4\ ^1S_0$	23.3940	23.4001	23.4382	5.923E+11	5.884E+11	5.704E+11
O II	$[1s]2p^4\ ^2P_{1/2} - 2p^3\ ^2D_{3/2}$	23.1144	23.1241	23.1788	2.534E+12	2.513E+12	2.407E+12
	$[1s]2p^4\ ^2P_{3/2} - 2p^3\ ^2D_{3/2}$	23.1159	23.1256	23.1802	2.541E+11	2.521E+11	2.426E+11
	$[1s]2p^4\ ^2P_{3/2} - 2p^3\ ^2D_{5/2}$	23.1159	23.1256	23.1803	2.342E+12	2.321E+12	2.224E+12
	$[1s]2p^4\ ^2S_{1/2} - 2p^3\ ^2P_{1/2}$	23.1204	23.1303	23.1858	6.302E+11	6.231E+11	5.890E+11
	$[1s]2p^4\ ^2S_{1/2} - 2p^3\ ^2P_{3/2}$	23.1204	23.1303	23.1858	1.372E+12	1.358E+12	1.289E+12
	$[1s]2p^4\ ^2D_{5/2} - 2p^3\ ^2D_{3/2}$	23.1636	23.1734	23.2286	9.126E+10	9.033E+10	8.579E+10
	$[1s]2p^4\ ^2D_{5/2} - 2p^3\ ^2D_{5/2}$	23.1636	23.1734	23.2287	1.389E+12	1.375E+12	1.307E+12
	$[1s]2p^4\ ^2D_{3/2} - 2p^3\ ^2D_{3/2}$	23.1638	23.1736	23.2288	1.376E+12	1.362E+12	1.293E+12
	$[1s]2p^4\ ^2D_{3/2} - 2p^3\ ^2D_{5/2}$	23.1638	23.1736	23.2289	1.259E+11	1.247E+11	1.191E+11
	$[1s]2p^4\ ^2P_{1/2} - 2p^3\ ^2P_{1/2}$	23.1759	23.1852	23.2376	1.054E+12	1.047E+12	1.013E+12
	$[1s]2p^4\ ^2P_{1/2} - 2p^3\ ^2P_{3/2}$	23.1759	23.1852	23.2376	5.130E+11	5.093E+11	4.910E+11
	$[1s]2p^4\ ^2P_{3/2} - 2p^3\ ^2P_{1/2}$	23.1774	23.1867	23.2390	2.676E+11	2.657E+11	2.563E+11
	$[1s]2p^4\ ^2P_{3/2} - 2p^3\ ^2P_{3/2}$	23.1774	23.1867	23.2391	1.237E+12	1.229E+12	1.188E+12
	$[1s]2p^4\ ^4P_{1/2} - 2p^3\ ^4S_{3/2}$	23.2124	23.2227	23.2807	9.524E+11	9.400E+11	8.801E+11
	$[1s]2p^4\ ^4P_{3/2} - 2p^3\ ^4S_{3/2}$	23.2131	23.2234	23.2814	9.523E+11	9.399E+11	8.801E+11
	$[1s]2p^4\ ^4P_{5/2} - 2p^3\ ^4S_{3/2}$	23.2143	23.2246	23.2825	9.521E+11	9.397E+11	8.800E+11
	$[1s]2p^4\ ^2D_{5/2} - 2p^3\ ^2P_{3/2}$	23.2254	23.2348	23.2877	5.013E+11	4.973E+11	4.781E+11
	$[1s]2p^4\ ^2D_{3/2} - 2p^3\ ^2P_{1/2}$	23.2256	23.2350	23.2879	3.980E+11	3.949E+11	3.800E+11
	$[1s]2p^4\ ^2D_{3/2} - 2p^3\ ^2P_{3/2}$	23.2256	23.2350	23.2879	8.319E+10	8.247E+10	7.888E+10
O III	$[1s]2p^3\ ^1P_1 - 2p^2\ ^1D_2$	22.8154	22.8267	22.8887	1.982E+12	1.967E+12	1.890E+12
	$[1s]2p^3\ ^3S_1 - 2p^2\ ^3P_0$	22.8748	22.8862	22.9485	4.582E+11	4.554E+11	4.428E+11
	$[1s]2p^3\ ^3S_1 - 2p^2\ ^3P_1$	22.8754	22.8868	22.9491	1.458E+12	1.449E+12	1.405E+12
	$[1s]2p^3\ ^3S_1 - 2p^2\ ^3P_2$	22.8766	22.8880	22.9503	2.736E+12	2.717E+12	2.621E+12
	$[1s]2p^3\ ^3P_1 - 2p^2\ ^3P_0$	22.8897	22.9011	22.9637	4.266E+11	4.225E+11	4.011E+11
	$[1s]2p^3\ ^3P_2 - 2p^2\ ^3P_1$	22.8902	22.9016	22.9642	2.660E+11	2.636E+11	2.515E+11
	$[1s]2p^3\ ^3P_0 - 2p^2\ ^3P_1$	22.8903	22.9017	22.9642	1.143E+12	1.132E+12	1.079E+12
	$[1s]2p^3\ ^3P_1 - 2p^2\ ^3P_1$	22.8903	22.9017	22.9643	3.956E+11	3.918E+11	3.702E+11
	$[1s]2p^3\ ^1D_2 - 2p^2\ ^1D_2$	22.8908	22.9021	22.9636	3.479E+12	3.455E+12	3.340E+12
	$[1s]2p^3\ ^3P_2 - 2p^2\ ^3P_2$	22.8914	22.9028	22.9653	8.768E+11	8.684E+11	8.277E+11
	$[1s]2p^3\ ^3P_1 - 2p^2\ ^3P_2$	22.8915	22.9029	22.9654	3.373E+11	3.342E+11	3.225E+11
	$[1s]2p^3\ ^1P_1 - 2p^2\ ^1S_0$	22.9227	22.9338	22.9943	1.535E+12	1.525E+12	1.480E+12
	$[1s]2p^3\ ^3D_1 - 2p^2\ ^3P_0$	22.9663	22.9776	23.0395	6.370E+11	6.319E+11	6.066E+11
	$[1s]2p^3\ ^3D_2 - 2p^2\ ^3P_1$	22.9669	22.9782	23.0400	8.592E+11	8.522E+11	8.181E+11
	$[1s]2p^3\ ^3D_1 - 2p^2\ ^3P_1$	22.9669	22.9782	23.0401	4.554E+11	4.518E+11	4.341E+11
	$[1s]2p^3\ ^3D_3 - 2p^2\ ^3P_2$	22.9680	22.9792	23.0410	1.119E+12	1.110E+12	1.067E+12
	$[1s]2p^3\ ^3D_2 - 2p^2\ ^3P_2$	22.9681	22.9794	23.0412	2.607E+11	2.587E+11	2.488E+11
	$[1s]2p^3\ ^3D_1 - 2p^2\ ^3P_2$	22.9682	22.9794	23.0413	2.776E+10	2.755E+10	2.651E+10

Notes. The plasma screening parameter μ is given in au, $\mu = 0$ denoting the isolated atomic system.

Table A.1. continued.

Ion	Transition	λ (Å)			$A(j,i)$ (s^{-1})		
		$\mu = 0.0$	$\mu = 0.1$	$\mu = 0.25$	$\mu = 0.0$	$\mu = 0.1$	$\mu = 0.25$
O IV	$[1s]2p^2\ ^2S_{1/2} - 2p\ ^2P_{1/2}$	22.5066	22.5192	22.5869	3.799E+11	3.772E+11	3.636E+11
	$[1s]2p^2\ ^2S_{1/2} - 2p\ ^2P_{3/2}$	22.5087	22.5214	22.5890	9.693E+11	9.607E+11	9.194E+11
	$[1s]2p^2\ ^2P_{3/2} - 2p\ ^2P_{1/2}$	22.5567	22.5695	22.6379	6.296E+11	6.259E+11	6.072E+11
	$[1s]2p^2\ ^2P_{1/2} - 2p\ ^2P_{1/2}$	22.5587	22.5716	22.6399	2.703E+12	2.686E+12	2.602E+12
	$[1s]2p^2\ ^2P_{3/2} - 2p\ ^2P_{3/2}$	22.5588	22.5717	22.6400	3.323E+12	3.303E+12	3.203E+12
	$[1s]2p^2\ ^2P_{1/2} - 2p\ ^2P_{3/2}$	22.5609	22.5737	22.6420	1.246E+12	1.239E+12	1.204E+12
	$[1s]2p^2\ ^2D_{3/2} - 2p\ ^2P_{1/2}$	22.6310	22.6437	22.7113	1.102E+12	1.094E+12	1.058E+12
	$[1s]2p^2\ ^2D_{5/2} - 2p\ ^2P_{3/2}$	22.6330	22.6457	22.7132	1.286E+12	1.277E+12	1.235E+12
	$[1s]2p^2\ ^2D_{3/2} - 2p\ ^2P_{3/2}$	22.6331	22.6458	22.7134	1.862E+11	1.850E+11	1.791E+11
O V	$[1s]2p\ ^1P_1 - 2s^2\ ^1S_0$	22.2088	22.2229	22.2960	2.884E+12	2.868E+12	2.786E+12
O VI	$[1s]2s2p\ ^2P_{3/2} - 2s\ ^2S_{1/2}$	21.7832	21.7998	21.8840	6.424E+11	6.368E+11	6.109E+11
	$[1s]2s2p\ ^2P_{1/2} - 2s\ ^2S_{1/2}$	21.7836	21.8002	21.8844	6.792E+11	6.735E+11	6.467E+11
	$[1s]2s2p\ ^2P_{3/2} - 2s\ ^2S_{1/2}$	21.9706	21.9860	22.0646	2.694E+12	2.680E+12	2.609E+12
	$[1s]2s2p\ ^2P_{1/2} - 2s\ ^2S_{1/2}$	21.9730	21.9884	22.0669	2.657E+12	2.643E+12	2.573E+12
O VII	$1s2p\ ^1P_1 - 1s^2\ ^1S_0$	21.5642	21.5821	21.6707	3.702E+12	3.680E+12	3.574E+12

Table A.2. Plasma environment effects on the energy and Auger widths of K-vacancy states in oxygen ions computed with MCDF.

Ion	Level	E (eV)			$A_a(j)$ (s^{-1})		
		$\mu = 0.0$	$\mu = 0.1$	$\mu = 0.25$	$\mu = 0.0$	$\mu = 0.1$	$\mu = 0.25$
O I	$[1s]2p^5\ ^3P_2$	530.39	530.20	529.14	2.606E+14	2.528E+14	2.104E+14
	$[1s]2p^5\ ^3P_1$	530.41	530.23	529.17	2.613E+14	2.536E+14	2.124E+14
	$[1s]2p^5\ ^3P_0$	530.43	530.24	529.18	2.587E+14	2.513E+14	2.110E+14
	$[1s]2p^5\ ^1P_1$	534.13	533.94	532.87	2.086E+14	2.037E+14	1.832E+14
O II	$[1s]2p^4\ ^4P_{5/2}$	534.08	533.85	532.52	2.489E+14	2.405E+14	2.202E+14
	$[1s]2p^4\ ^4P_{3/2}$	534.11	533.87	532.54	2.474E+14	2.392E+14	2.191E+14
	$[1s]2p^4\ ^4P_{1/2}$	534.12	533.89	532.55	2.475E+14	2.394E+14	2.194E+14
	$[1s]2p^4\ ^2D_{3/2}$	539.22	538.96	537.51	3.004E+14	2.928E+14	2.680E+14
	$[1s]2p^4\ ^2D_{5/2}$	539.22	538.96	537.51	3.011E+14	2.935E+14	2.686E+14
	$[1s]2p^4\ ^2P_{3/2}$	540.33	540.07	538.63	2.050E+14	1.975E+14	1.804E+14
	$[1s]2p^4\ ^2P_{1/2}$	540.37	540.11	538.66	2.041E+14	1.969E+14	1.798E+14
	$[1s]2p^4\ ^2S_{1/2}$	541.65	541.38	539.85	3.014E+14	2.924E+14	2.578E+14
O III	$[1s]2p^3\ ^3D_1$	539.86	539.59	538.14	2.969E+14	2.903E+14	2.719E+14
	$[1s]2p^3\ ^3D_2$	539.86	539.59	538.14	2.957E+14	2.891E+14	2.709E+14
	$[1s]2p^3\ ^3D_3$	539.86	539.59	538.15	2.974E+14	2.908E+14	2.724E+14
	$[1s]2p^3\ ^3P_1$	541.66	541.39	539.92	2.746E+14	2.682E+14	2.500E+14
	$[1s]2p^3\ ^3P_0$	541.66	541.39	539.92	2.733E+14	2.669E+14	2.488E+14
	$[1s]2p^3\ ^3P_2$	541.66	541.39	539.92	2.746E+14	2.681E+14	2.499E+14
	$[1s]2p^3\ ^3S_1$	542.02	541.74	540.27	1.050E+14	1.031E+14	9.827E+13
	$[1s]2p^3\ ^1D_2$	544.59	544.30	542.76	2.562E+14	2.505E+14	2.350E+14
	$[1s]2p^3\ ^1P_1$	546.38	546.09	544.52	2.389E+14	2.333E+14	2.177E+14
O IV	$[1s]2p^2\ ^2D_{3/2}$	547.85	547.54	545.91	2.617E+14	2.552E+14	2.392E+14
	$[1s]2p^2\ ^2D_{5/2}$	547.86	547.55	545.92	2.622E+14	2.556E+14	2.395E+14
	$[1s]2p^2\ ^2P_{1/2}$	549.61	549.29	547.63	1.054E+14	1.033E+14	9.766E+13
	$[1s]2p^2\ ^2P_{3/2}$	549.66	549.34	547.68	1.054E+14	1.032E+14	9.762E+13
	$[1s]2p^2\ ^2S_{1/2}$	550.88	550.57	548.92	2.239E+14	2.179E+14	2.029E+14
O V	$[1s]2p\ ^1P_1$	558.26	557.92	556.08	1.196E+14	1.168E+14	1.095E+14
O VI	$[1s]2s2p\ ^2P_{1/2}$	564.25	563.87	561.86	3.902E+13	3.677E+13	3.360E+13
	$[1s]2s2p\ ^2P_{3/2}$	564.32	563.93	561.92	3.651E+13	3.434E+13	3.128E+13
	$[1s]2s2p\ ^2P_{1/2}$	569.16	568.73	566.55	9.593E+13	9.544E+13	9.314E+13
	$[1s]2s2p\ ^2P_{3/2}$	569.17	568.74	566.56	9.701E+13	9.649E+13	9.414E+13

Notes. The plasma screening parameter μ is given in au, $\mu = 0$ denoting the isolated atomic system.